Balancing Flying Capacitor Multilevel Converters with Coupled Inductors: Multi-Resonant Dynamics

Daniel H. Zhou, *Student Member, IEEE* and Minjie Chen, *Senior Member, IEEE*

***Abstract*—This paper investigates dynamic balancing of flying capacitor multilevel (FCML) converters with coupled inductors. Coupled inductors help to reduce the ripple current, accelerate transient response, and balance the flying capacitors of FCML converters at steady-state. However, coupled inductors also change the dynamic balancing properties compared to uncoupled inductors, and these principles must be understood for robust design. As an extension of a previously developed feedback mechanism for understanding the steady-state behaviors of coupled inductors in FCML converters, this paper derives models of coupled inductor FCML converters in dynamic operation, revealing several key insights: (i) the multi-resonant behavior of large-order FCML converters and their dependence on the initial conditions, (ii) how power dissipation relates to balancing speed, and (iii) the relation between multiphase and multilevel FCML balancing. The insights uncovered by this paper can provide useful guidelines for designing multi-phase self-balanced FCML converters with coupled inductors.**

***Index Terms*—flying capacitor multilevel converter, coupled inductors, natural balancing, charge balancing, voltage balancing, multi-resonance**

I. Introduction

Flying capacitor multilevel (FCML) converters [2] are an important class of converters that leverage interleaved switching devices to generate multiple switching levels, reducing current ripple and transient response time in sensitive applications such as CPU voltage regulators [3], [4], envelope trackers, and power amplifiers [5], [6], especially as the power level increases [7]–[11]. Compared to traditional buck converters, FCML converters benefit from replacing inductor volume with more energy-dense flying capacitors and switches with lower blocking voltages [12].

However, the advantages of FCML converters are predicated on the flying capacitor voltages being at their balanced levels. If they are not balanced, the switching levels will be corrupted, which increases output distortion, switch stress, and current ripple [13]–[16]. In practice, this limitation has posed a major barrier to the adoption of FCML converters despite their theoretical benefits [17]. As a result, considerable effort has been made to investigate how FCML converters become unbalanced and what mechanisms can be used to balance them. FCML balancing is complicated by the fact that it is a fundamentally higher-order effect, as established in seminal early works such as [13], [15], [16], thus precluding the use of standard state-space averaging methods. This first generation of work used frequency domain decomposition of the switching waveforms to establish the existence of natural balancing, a property possessed by practical FCML converters that have parasitic losses. Natural balancing essentially refers to the process where flying capacitor imbalances dissipate themselves by the losses they cause in the switches, load, or output network.

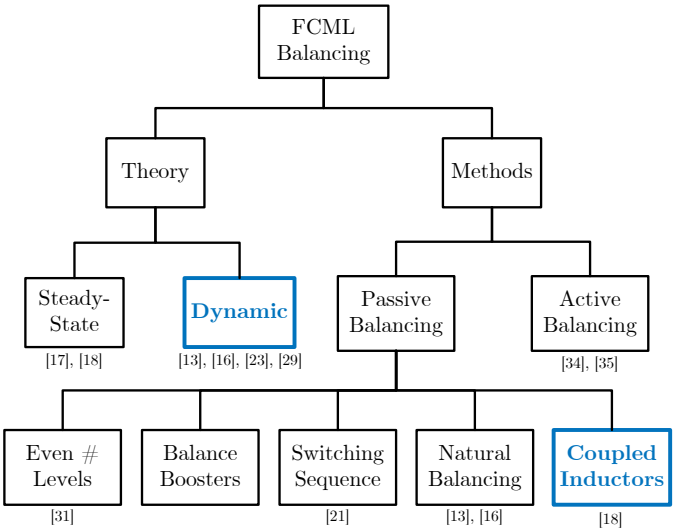

Fig. 1. Chart of selected research areas in FCML converter balancing with selected references. Coupled inductors represent a new branch of techniques for passively balancing FCML converters which can be used together with other techniques. Extended from the steady-state discussions in [18], this paper investigates the dynamic behavior of FCML converters with coupled inductors.

These results, while thorough, were relatively complex, and the second generation of FCML balancing analyses attempted to rectify this by using time-domain methods based on "stitching" piece-wise linear circuit solutions for every switching state of the converter during a full period [19]–[21]. These methods produce results consistent with previous frequency domain analysis and emphasized the importance of the PWM (pulse-width modulation) switching scheme to the balancing behavior, thus suggesting the possibility of improving balancing by optimal sequencing of redundant switch states [21]. Two drawbacks of the time-domain "stitching" methods are their relative informality and the high computational cost.

The current generation of balancing research has built upon, formalized, and refined prior results [17], [22]–[31]. These works and others improve the state-space models of FCML balancing, in addition to proving how balancing loses

This paper is an extension of a paper published at the 2023 Energy Conversion Congress & Expo (ECCE) [1].

Daniel H. Zhou and Minjie Chen are with the Department of Electrical Engineering and Andlinger Center for Energy and the Environment at Princeton University, Princeton, NJ, 08540, USA.

This work was supported in part by NSF CAREER Award No. 1847365, and in part by the NSERC PGS-D Award No. 557270-2021.

robustness or fails at nominal conversion ratios and with converters with an odd number of levels [30], [31]. Many practical aspects of FCML balancing, such as the impact of switch parasitics [24], high-speed operation [8], [32] and start-up/shut-down dynamics [33] have also been investigated. Because of these developments, FCML balancing analysis now includes the dynamic (what happens when the flying capacitors are not balanced and evolve towards equilibrium) and steady-state (the imbalance that exists even at equilibrium due to some persistent disturbance) [17], [18], [29], [31]. FCML balancing also spans passive, natural, and dissipative methods, along with active balancing where flying capacitor voltages are measured or estimated and actively balanced [34], [35]. Some of these general branches of research are outlined in Fig. 1.

Coupled inductors are an effective tool for balancing FCML converters with many levels and many phases by generating circulating currents at steady-state which compensate for disturbances [18], [36], while also improving the ripple and transient properties of the converter [37]–[39]. However, coupled inductors also affect the balancing dynamics, and it is not fully understood how this changes the converter's behavior during important conditions such as start-up, shut-down, and high-speed operation [32]. Here, we develop two analytical frameworks to explain the dynamics of coupled inductor FCML balancing: first, a model based on power dissipation that produces closed-form solutions for simple converters, and second, a state-space model that captures the multi-resonant balancing dynamics of coupled inductor FCML converters. This work makes several contributions to FCML balancing dynamics, both with and without coupled inductors, by investigating:

- How balancing dynamics can be explained through the loss-context and by tracking the average power being dissipated because of the imbalance.
- The similarity of balancing dynamics for a multiphase and multilevel FCML converter.
- How the initial condition of an unbalanced converter can dramatically affect the balancing dynamics and speed.

The rest of this paper is organized as follows: section II reviews the fundamentals of coupled inductor FCML converters. Section III develops a power dissipation model of simple FCML converters. Section IV extends state-space models of FCML converter balancing to coupled inductors. Finally, the results are experimentally verified in section V and concluded in section VI.

II. Review of Coupled Inductor FCML Converters

A two-phase, three-level FCML converter with coupled inductors is shown in Fig. 2. The two FCML phases each have two pairs of complementary switches and one flying capacitor with an ideal balanced voltage of half the input voltage. The switches in one phase are operated with a 180° phase shift such that two evenly spaced pulses are produced at the switch nodes, as shown in Fig. 4. The two FCML converters are themselves 90° phase shifted from each other, thus producing four evenly spaced pulses that minimize ripple. This operational scheme is known as phase-shifted pulse width modulation (PS-PWM).

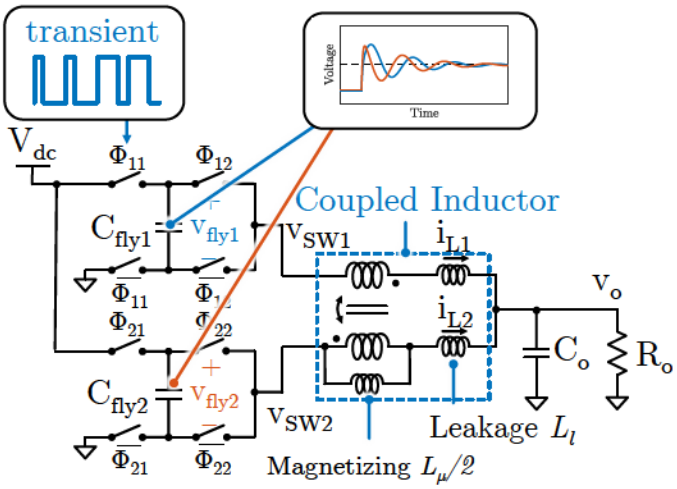

Fig. 2. Schematic of two-phase, three-level FCML converter with coupled inductors. After a transient unbalances the flying capacitors, they balance back to equilibrium due to losses in the circuit.

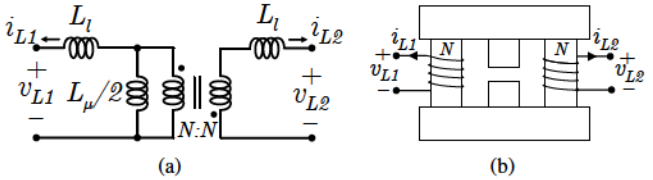

Fig. 3. (a) Schematic and (b) diagram of a two-phase coupled inductor parameterized using leakage and magnetizing inductance.

The inductors in Fig. 2 are coupled, meaning the windings share a single core as illustrated in Fig. 3(b). By sharing the magnetic flux paths between the two phases, the voltage applied to one coil will affect the current in the other. This effect is leveraged to present a low inductance during common-mode transient events and a high inductance to steady-state ripple current [39], [40]. These inductances are represented by the leakage (L_l) and magnetizing (L_μ) inductances of the coupled inductor. As the inductors are more tightly coupled, the magnetizing inductance increases. As the leakage inductance decreases, the transient response is accelerated. However, it is important to switch all phases with equal phase shift when using tightly coupled inductors, as failure to do so will present a very low inductance to some phases at steady-state. In this work, we assume the inductors are fully coupled, meaning the magnetizing inductance is infinite and, as shown in the schematic in Fig. 3(a), the currents in both phases of the coupled inductor are equal to

$$\frac{\mathrm{d}i_{L1}}{\mathrm{d}t} = \frac{\mathrm{d}i_{L2}}{\mathrm{d}t} = \frac{v_{L1} + v_{L2}}{2L_l}. \tag{1}$$

This is also shown in the waveforms in Fig. 4.

To analyze the balancing behavior of coupled inductors in FCML converters with multiple phases and levels, we define the number of phases as M and the number of flying capacitors as K, meaning each phase is a $(K+2)$-level FCML converter since each flying capacitor adds one more switching voltage level in addition to GND and V_{dc}. We denote the flying capacitor voltages as $v_{fly}^{(\text{phase \#m, cap \#k})}$, or for brevity, $v_{fly}^{(m,k)}$,

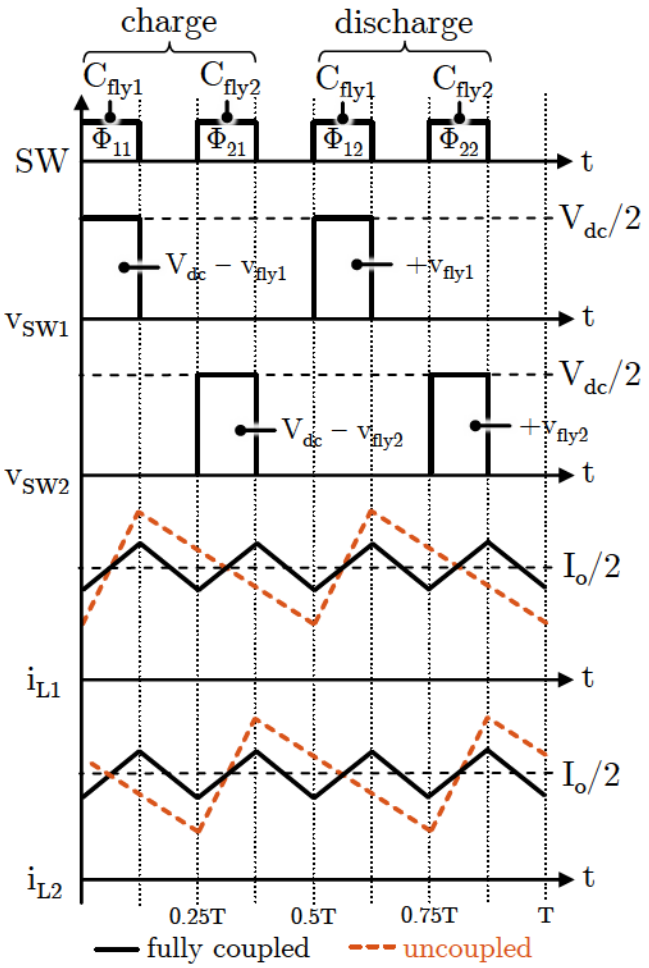

Fig. 4. Switching waveforms of the two-phase, three-level FCML converter in Fig. 2 with PS-PWM and $d = 0.125$. If the inductors are fully coupled, the per-phase currents are equal both in average and in ripple.

where $m = 1, \ldots, M$ and $k = 1, \ldots, K$ are the indices identifying the phase and capacitor. The capacitor closest to the input source has the index $k = 1$.

In developing the two models, we make frequent use of the small-signal imbalance voltages and currents of the FCML converter [18]. This allows us to focus on the balancing behavior of interest. In this work, we use tildes to denote small-signal imbalance components of interest. For an M-phase, $(K+2)$-level converter, there are $M \times K$ total flying capacitors with voltages

$$v_{\text{fly}}^{(m,k)} = v_{\text{fly, balanced}}^{(m,k)} + \tilde{v}_{\text{fly}}^{(m,k)}, \tag{2}$$

split into balanced and unbalanced components. The ideally balanced voltage of each flying capacitor is

$$v_{\text{fly, balanced}}^{(\text{m, k})} = V_{\text{dc}} \frac{K+1-k}{K+1}, \tag{3}$$

which is the voltage that they return to under the influence of natural balancing. External disturbances such as input impedances, transient events, or timing mismatches can cause the flying capacitor voltages to leave equilibrium [17], [18]. More detailed analyses of FCML converter operation can be found in works such as [2], [14], [18], [41], and more detailed models of coupled inductors can be found in [39].

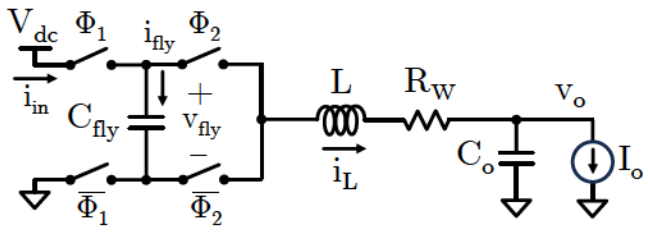

Fig. 5. Schematic of a three-level FCML converter.

III. Power Dissipation Model of FCML Balancing

A. Motivation

By studying FCML dynamics, we wish to understand how the converter transitions from an unbalanced initial condition to a balanced equilibrium, and what factors affect the speed and stability of said transition. As introduced in section I, natural balancing occurs in FCML converters because imbalanced flying capacitors cause additional losses in the converter that balance the system over time. Many factors such as the switching frequency and inductor quality factor affect the magnitude of loss and thus the balancing speed; we term these factors the "loss-context" of the converter. While the qualitative impact of these factors have been understood from early studies [2], [16], [42] onward, their quantitative relation to balancing is less clear since most current dynamic models are not derived from the root cause of balancing, which is power dissipation.

In this section, we model FCML balancing dynamics by directly calculating the power dissipation caused by unbalancing and the balancing dynamics that result. Using this method, we reveal the direct analytical link between the loss-context and balancing speed of simple one- and two-phase three-level FCML converters, adding depth and support to existing research results.

B. Assumptions

The analytical methods are tenable only with several important simplifying assumptions. They are enumerated here, along with the importance and justification of each.

1) The flying capacitors C_{fly} are large enough such that the flying capacitor voltages are approximately constant in one period. This simplifies the period-by-period discretization of the dynamics and is valid because practical converters need small flying capacitor voltage ripple to maintain a stable switch node voltage level and to protect the switches from overvoltage. The output capacitance is assumed to be large enough such that the output voltage is approximately constant.
2) The quality factor of the inductor is high and the current ramps up and down approximately linearly. This simplifies the current and loss calculations and is valid because practical converters usually have high inductor quality factor for high efficiency.
3) The loss is represented by a winding resistor R_w. The analysis is limited to loss sources that can be reasonably represented in this way and is not applicable to, for example, nonlinear loss sources.

TABLE I
PLECS SIMULATION OF BALANCING TIME [MS] VS. LARGE SIGNAL INPUT/OUTPUT CONDITIONS

I_o [A] \ V_{dc} [V]	4	8	12	16
0	120.0	120.0	120.2	120.2
5	121.5	121.6	121.7	121.8
10	123.0	123.1	123.2	123.2
15	124.5	124.6	124.6	124.7

4) When analyzing coupled inductor converters, they are assumed to be fully coupled. This simplifies the equivalent circuits and current calculations. A justification is provided in section IV-C.

C. Model Derivation

Our derivation stems from the observation that three-level converters generally balance exponentially with a time constant that does not depend on the input voltage level or output current, as exemplified by the PLECS simulation results in Table I for a simple three-level converter (Fig. 5) with $f_{sw} = 500$ kHz, $d = 0.25$, $C_{fly} = 50$ μF, $L = 1$ μH, $R_w = 10$ mΩ, $C_o = 100$ μF, and an initial 2 V imbalance. The apparent independence of balancing speed from large signal conditions suggest that the power dissipation causing balancing is dependent only on the imbalance magnitude. To investigate this, we begin by noting the inductor current can be split into three components shown in Fig. 6: the load current I_o, a ripple component i_{ripple}, and the current induced by the unbalanced flying capacitors $\tilde{i}_L$, the latter of which is only possessed by the unbalanced system. The average value of the ripple and imbalance component are both assumed to be zero. The instantaneous loss in the resistor R_w is therefore

$$P_{R_w}(t) = R_w i_L(t)^2 = R_w \left[I_o + i_{ripple}(t) + \tilde{i}_L(t)\right]^2. \quad (4)$$

The instantaneous power dissipation changes with time and is evidently dependent on the large signal conditions. To simplify the analysis, we discretize the continuous balancing system into steps of duration T. We do this by assuming the flying capacitor voltage is constant over the period T (large C_{fly}), then update it at the end of every period using the average power dissipation over the period. This discretization is valid since the capacitor balancing dynamics in practical converters with large C_{fly} and small losses are much slower than the period. The average power dissipation in the resistor over a period is

$$\overline{P_{R_w}}(t) = R_w \left\langle i_L(t)^2 \right\rangle, \quad (5)$$

where $\langle x(t) \rangle = \frac{1}{T}\int_t^{t+T} x(\zeta)\,\mathrm{d}\zeta$ is the average of a function over one period. We expand and simplify eq. (5) to find

$$\begin{aligned}\overline{P_{R_w}}(t) &= R_w \left\langle \left[I_o + i_{ripple}(t) + \tilde{i}_L(t)\right]^2 \right\rangle \\ &= R_w I_o^2 + R_w \left\langle i_{ripple}(t)^2 \right\rangle + R_w \left\langle \tilde{i}_L(t)^2 \right\rangle \\ &\quad + 2R_w I_o \left\langle i_{ripple}(t) \right\rangle + 2R_w I_o \left\langle \tilde{i}_L(t) \right\rangle \\ &\quad + 2R_w \left\langle i_{ripple}(t)\tilde{i}_L(t) \right\rangle. \end{aligned} \quad (6)$$

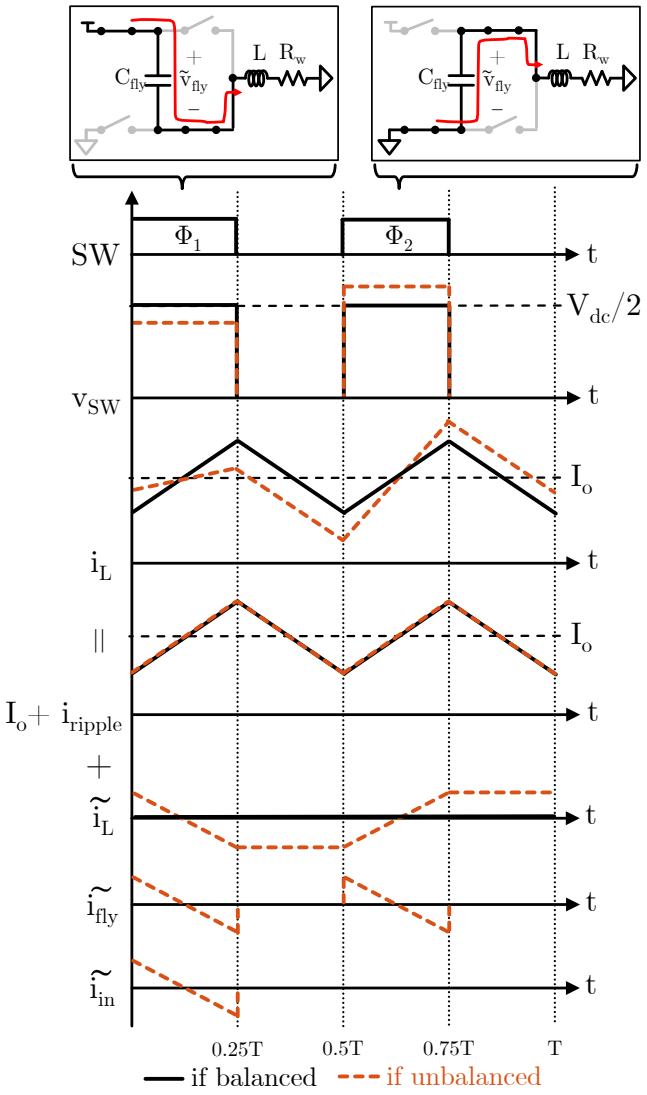

Fig. 6. Large- and small-signal components of the inductor current ripple in a balanced and unbalanced FCML converter.

Eq. (6) can be simplified by noting the average of the ripple and imbalance components over a period are zero. Furthermore, $\left\langle i_{ripple}(t)\tilde{i}_L(t) \right\rangle = 0$ since the two functions are orthogonal when averaged over a period. This can be inspected in Fig. 6; both functions have zero average, are symmetric, but the ripple current has twice the frequency. Therefore, the average power dissipation is

$$\overline{P_{R_w}}(t) = R_w I_o^2 + R_w \left\langle i_{ripple}(t)^2 \right\rangle + R_w \left\langle \tilde{i}_L(t)^2 \right\rangle. \quad (7)$$

The difference between the average power dissipation in a balanced $\left(\tilde{i}_L = 0\right)$ and unbalanced $\left(\tilde{i}_L \neq 0\right)$ converter is $R_w \left\langle \tilde{i}_L(t)^2 \right\rangle$, which depends only on the imbalanced components and not on the steady-state load or ripple. In addition to the power dissipated in R_w, we see by inspection of Fig. 5, there are two more power sinks (the load and charging C_{fly}) and one power source (V_{dc}) in the converter. During each period, the power sources and sinks must cancel to

$$\overline{P_{in}}(t) - \overline{P_{R_w}}(t) - \overline{P_{fly}}(t) - \overline{P_o}(t) = 0. \quad (8)$$

Here, the average output power is

$$\overline{P_{\text{o}}}(t) = \langle I_o(dV_{\text{dc}} - i_L(t)R_w)\rangle = dV_{\text{dc}}I_o - R_w I_o^2, \quad (9)$$

and the average input power is

$$\overline{P_{\text{in}}}(t) = \langle V_{\text{dc}} i_{\text{in}}(t)\rangle = V_{\text{dc}}\left(dI_o + \left\langle i_{\text{ripple}}(t) + \tilde{i}_L(t)\right\rangle_t^{t+dT}\right), \quad (10)$$

where $\langle x(t)\rangle_a^b = \frac{1}{T}\int_a^b x(t)\,\mathrm{d}t$. The average power into the flying capacitor, following from Fig. 6, is

$$\begin{aligned}\overline{P_{\text{fly}}}(t) &= \langle v_{\text{fly}}(t) i_{\text{fly}}(t)\rangle \\ &= v_{\text{fly}}(t)\left(\langle i_L(t)\rangle_t^{t+dT} - \langle i_L(t)\rangle_{0.5T}^{(0.5+d)T}\right) \\ &= v_{\text{fly}}(t)\left(2\left\langle \tilde{i}_L(t)\right\rangle_t^{t+dT}\right), \end{aligned} \quad (11)$$

where $v_{\text{fly}}(t) = \frac{V_{\text{dc}}}{2} + \tilde{v}_{\text{fly}}(t)$. Since the flying capacitor sees the inductor current twice per period in opposite directions and equal durations, the ripple and load component cancel out in average. Only the imbalance component causes any average power transfer to the flying capacitor. Substituting eqs. (7), (9), (10), and (11) into eq. (8) yields

$$\begin{aligned} &V_{\text{dc}}\left\langle i_{\text{ripple}}\right\rangle_t^{t+dT} - R_w\left\langle i_{\text{ripple}}(t)^2\right\rangle \\ &- 2\tilde{v}_{\text{fly}}\left\langle \tilde{i}_L(t)\right\rangle_t^{t+dT} - R_w\left\langle \tilde{i}_L(t)^2\right\rangle = 0 \end{aligned} \quad (12)$$

after canceling most terms. Eq. 12 must be satisfied for all values of the imbalance, even when the converter is balanced and $\tilde{i}_L(t) = 0$. This implies that

$$V_{\text{dc}}\left\langle i_{\text{ripple}}\right\rangle_t^{t+dT} = R_w\left\langle i_{\text{ripple}}(t)^2\right\rangle, \quad (13)$$

because the dissipation caused by the ripple current in R_w must be compensated by more power coming from the input. If we then substitute eq. (12) and (13) into eq. (11), we conclude that the average power into the flying capacitor is

$$\overline{P_{\text{fly}}}(t) = -v_{\text{fly}}(t) \times \frac{R_w\left\langle \tilde{i}_L(t)^2\right\rangle}{\tilde{v}_{\text{fly}}(t)} \quad (14)$$

We now calculate the difference in average power dissipation between a balanced and unbalanced converter

$$\begin{aligned} R_w\left\langle \tilde{i}_L(t)^2\right\rangle &= \frac{R_w}{T}\int_0^T \tilde{i}_L(t)^2 \mathrm{d}t \\ &= \frac{R_w T^2 d^2(3-4d)\tilde{v}_{\text{fly}}(t)^2}{12L^2} = \frac{\tilde{v}_{\text{fly}}(t)^2}{R_{\text{eff}}}, \end{aligned} \quad (15)$$

for $d \le 0.5$ (mirrored for $d > 0.5$), with details in Appendix I. $R_{\text{eff}} = \frac{12L^2}{R_w T^2 d^2(3-4d)}$ is the effective resistance that takes into account all relevant loss-context factors: the series resistance R_w, switching frequency, duty cycle, and inductance. A final substitution into (14) yields

$$\overline{P_{\text{fly}}}(t) = -\frac{v_{\text{fly}}(t) \times \tilde{v}_{\text{fly}}(t)}{R_{\text{eff}}}, \quad (16)$$

the average power into the flying capacitor, which depends on both the balanced and unbalanced components of the flying capacitor voltage. Having found the average power into the flying capacitor, we now consider energy stored in it,

$$E_{\text{fly}}(t) = \frac{1}{2}C_{\text{fly}} v_{\text{fly}}(t)^2. \quad (17)$$

The change in energy in flying capacitor energy between periods is

$$\Delta_T[E_{\text{fly}}(t)] = \overline{P_{\text{fly}}}(t) \times T, \quad (18)$$

where $\Delta_T[E_{\text{fly}}(t)] = E_{\text{fly}}(t+T) - E_{\text{fly}}(t)$ denotes the forward difference of a function. Expanding (18) with eqs. (17) and (16) yields

$$\begin{aligned} \frac{1}{2}C_{\text{fly}}\Delta_T[v_{\text{fly}}(t)^2] &= -\frac{v_{\text{fly}}(t) \times \tilde{v}_{\text{fly}}(t)}{R_{\text{eff}}} \times T \\ \frac{V_{\text{dc}}\Delta_T[\tilde{v}_{\text{fly}}(t)]}{T} + \frac{\Delta_T[\tilde{v}_{\text{fly}}(t)^2]}{T} &= -\frac{2v_{\text{fly}}(t) \times \tilde{v}_{\text{fly}}(t)}{C_{\text{fly}}R_{\text{eff}}} \\ V_{\text{dc}}\frac{\mathrm{d}\tilde{v}_{\text{fly}}(t)}{\mathrm{d}t} + \frac{\mathrm{d}\tilde{v}_{\text{fly}}(t)^2}{\mathrm{d}t} &\approx -V_{\text{dc}}\frac{\tilde{v}_{\text{fly}}(t)}{C_{\text{fly}}R_{\text{eff}}} - 2\frac{\tilde{v}_{\text{fly}}(t)^2}{C_{\text{fly}}R_{\text{eff}}} \end{aligned} \quad (19)$$

Here, we apply the forward approximation of the derivative $\frac{\Delta_T[x(t)]}{T} \approx \frac{\mathrm{d}x(t)}{\mathrm{d}t}$. The solution for the flying capacitor imbalance voltage that satisfies (19) is

$$\tilde{v}_{\text{fly}}(t) = \tilde{v}_{\text{fly}}(0)e^{-\frac{t}{C_{\text{fly}}R_{\text{eff}}}}, \quad (20)$$

Eq. (20) implies that the imbalance voltage decays exponentially, matching existing literature, with time constant $\tau_{M=1} = C_{\text{fly}}R_{\text{eff}} = \frac{12C_{\text{fly}}L^2}{R_w T^2 d^2(3-4d)}$. The dependence on the loss-context is clear. The balancing time is faster with smaller flying capacitors or high loss, through low quality factor, lower switching frequency (leading to higher peak currents), or with higher duty cycle (such that the flying capacitors are connected to the output for a longer part of the period.) If we substitute the parameters used for the simulations in Table I, eq. (20) predicts a balancing time of 120 ms.

The PLECS simulation results in Fig, 7 verify the mathematical derivations with $V_{\text{dc}} = 16$ V, $I_o = 5$ A, and the same component parameters as before. Two parallel simulations are performed, one with a balanced flying capacitor, and one with a 2 V starting imbalance. This generates balanced and unbalanced flying capacitor voltages ($v_{\text{fly,u}}(t)$, $v_{\text{fly,b}}(t)$) and inductor currents ($i_{L,u}(t)$, $i_{L,b}(t)$), the unbalanced versions of which are plotted. The third plot verifies the average power formulations of equations (7) and (15). The fourth plot verifies both sides of the energy step equation (18).

D. Comparison to Coupled Inductors

The power dissipation method also applies to the two-phase, three-level coupled FCML converter illustrated in Fig. 2 applying the same assumptions as before. For the two-phase converter, there are two flying capacitors causing an average power loss

$$R_w\left\langle \tilde{i}_L(t)^2\right\rangle = \frac{R_w T^2 d^2(3-4d)\|\tilde{\mathbf{v}}_{\text{fly}}\|^2}{24L_l^2} = \frac{\|\tilde{\mathbf{v}}_{\text{fly}}\|^2}{R_{\text{eff}}}, \quad (21)$$

where $\tilde{\mathbf{v}}_{\text{fly}}$ is a vector of the imbalance voltages and $\|.\|$ is the Euclidean norm. The average power loss over a period only depends on the normalized imbalance voltage $\|\tilde{\mathbf{v}}_{\text{fly}}\|$. This is important since it enables us to solve an power-balance equation by treating $\|\tilde{\mathbf{v}}_{\text{fly}}\|^2$ as the dynamic variable:

$$\|\tilde{\mathbf{v}}_{\text{fly}}(t)\| = \|\tilde{\mathbf{v}}_{\text{fly}}(0)\|e^{-\frac{t}{C_{\text{fly}}R_{\text{eff}}}} \quad (22)$$

The normalized imbalance of the two-phase converter therefore decays with time constant $\tau_{M=2} = \frac{24C_{\text{fly}}L_l^2}{R_w T^2 d^2(3-4d)}$, which

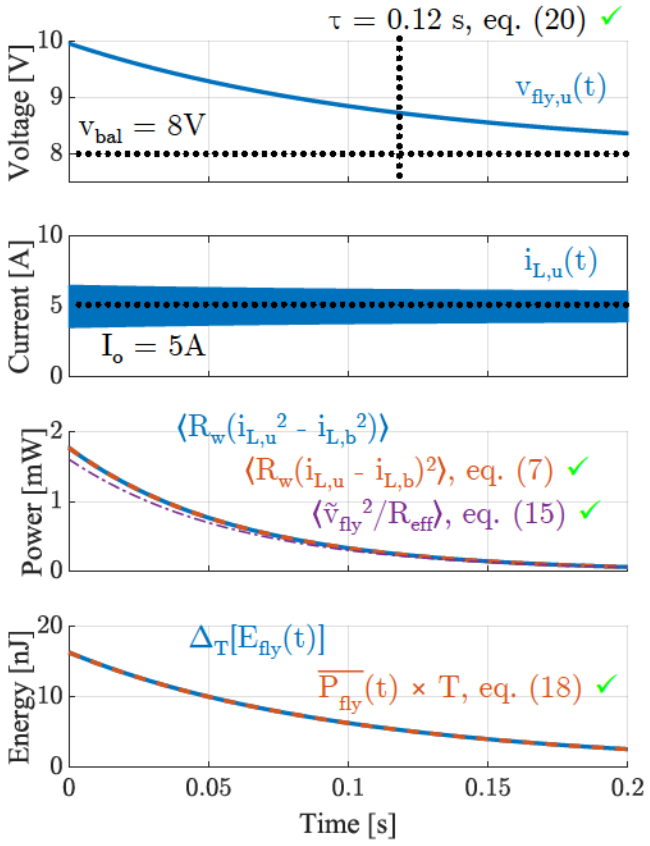

Fig. 7. PLECS simulation verification of key equations in derivation of the power dissipation model of balancing.

is identical to the one-phase case except depending on the leakage inductance L_l and with a different scaling factor. The fundamental natural balancing mechanism acting on the circuits is the same. The leakage inductance can be designed to be much smaller than the discrete inductance of an uncoupled converter due to the ripple reduction and cancellation effect of interleaving and coupling [39]. The maximum ripple across the duty cycle range of a coupled and uncoupled converter will be the same if the leakage inductance is designed to be $L_l = \frac{L}{M^2}$ [1]. In this case, the ratio between the balancing times is

$$\frac{\tau_{M=2}}{\tau_{M=1}} = \frac{1}{8}. \tag{23}$$

A two-phase coupled inductor converter can balance eight times faster than an uncoupled converter without changing the ripple. Even if the leakage inductance is not minimized, it can still accelerate the dynamics of a coupled converter significantly.

By solving for the power dissipation directly, this model reveals the fundamental mechanism of natural balancing. Our results confirm those in previous literature [16] and emphasize the importance of loss on the dynamics: more generally than just the actual loss source (winding resistance, core loss, switching loss, etc.), the dynamics depend on the loss-context. If the condition is lossy, such as a low switching frequency that generates high peak square currents, the dynamics will be faster.

The limitation of the power dissipation model is that it cannot be used for more complex coupled FCML converters. While they still have the same fundamental balancing mechanism, we cannot generally express the loss as a function of the normalized imbalance only, and thus cannot write a differential equation like in eq. (22). This is because there are generally multiple dynamic modes for more complex converters and the balancing dynamics depend not only on the normalized imbalance, but also on the individual voltages. To explore this phenomenon, we develop a dynamic model based on formal state-space analysis [41] for coupled inductor FCML converters in the next section.

IV. Multi-Resonant FCML Balancing Dynamics

To address the shortcomings of the power dissipation model, we develop a more general state-space dynamic model in this section. Many prior works have developed comprehensive state-space models for the balancing dynamics of FCML converters with a single phase [12], [22], [26], [30], which we we extend coupled inductor FCML converters. Since the mathematical modifications from uncoupled FCML models in previous works [41] are minor, the details are contained in Appendix II. The steps to derive a generalized dynamic model of an FCML converter typically consists of [41] (i) describing the switching states, (ii) reducing the circuit to an equivalent circuit at each switching state, (iii) solving the equivalent circuit for each sub-period, (iv) combining the sub-period solutions, and (v) analyzing the dynamics of the combined solution.

In developing this model, we reveal the multi-resonant dynamic behavior of larger-order coupled FCML converters ($M \geq 4$), where there exist multiple balancing modes of drastically different speed that are excited depending on the initial conditions of the imbalance.

A. State-Space Model for Coupled Inductor FCML Balancing Dynamics

The main adaptation required from previous models is the reduction of the coupled inductor circuit. As before, we assume fully coupled inductors. Fig. 8 shows the reduction of the full circuit schematic for a given switching state. For a generalized M-phase, $(K+2)$-level converter, there will be a total of $2M(K+1)$ switching states, during each of which a set of flying capacitors are connected to the output (example shown in (a)). (b) reduces the circuit to its small-signal imbalance components. Because of the coupled inductor, we must add step (c), where fully coupled inductors are assumed; therefore, the current in each phase is equal, and the multiphase circuit is equivalent to placing all the capacitors in series since they all charge/discharge with the same current. Finally, the circuit is reduced to (d) with one equivalent capacitance. Of interest is the fact that if the inductors are fully coupled, adding more phases has a very similar effect to adding more levels on the balancing dynamics. The equivalent circuit is still a sum of capacitors connected in series.

The equivalent circuit in Fig. 8(d) is solved for each of the switching sub-periods, then each sub-period solution is

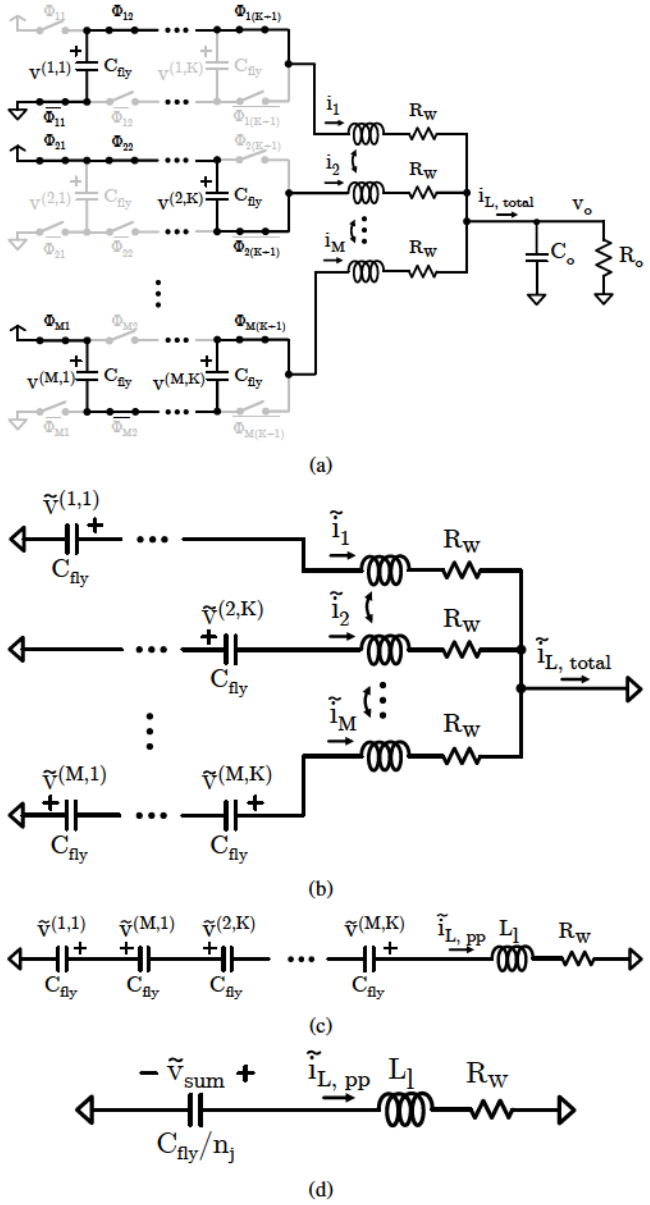

Fig. 8. (a) Full schematic for a given switching state, before reduction. (b) Schematic with only small-signal imbalances. (c) Coupled inductor reduction into one equivalent phase. (d) Final reduced schematic with only one equivalent capacitance, inductance, and resistance.

combined to produce a discrete state transition matrix that updates the state variables through a switching period

$$\tilde{\mathbf{x}}(T) = \mathbf{T}_{\text{full}}\tilde{\mathbf{x}}(0), \tag{24}$$

which we then convert using the forward approximation of the derivative to derive a continuous model

$$\frac{\mathrm{d}\tilde{\mathbf{x}}(t)}{\mathrm{d}t} \approx \mathbf{A}\tilde{\mathbf{x}}(t), \tag{25}$$

where

$$\tilde{\mathbf{x}} = \begin{bmatrix} \tilde{v}_{\text{fly}}^{(1,1)} & \cdots & \tilde{v}_{\text{fly}}^{(1,K)} & \tilde{v}_{\text{fly}}^{(2,1)} & \cdots & \tilde{v}_{\text{fly}}^{(M,K)} & \tilde{i}_L \end{bmatrix}^{\mathrm{T}} \tag{26}$$

is a vector of the state variables. The details of this derivation are contained in Appendix II. The internal state-space

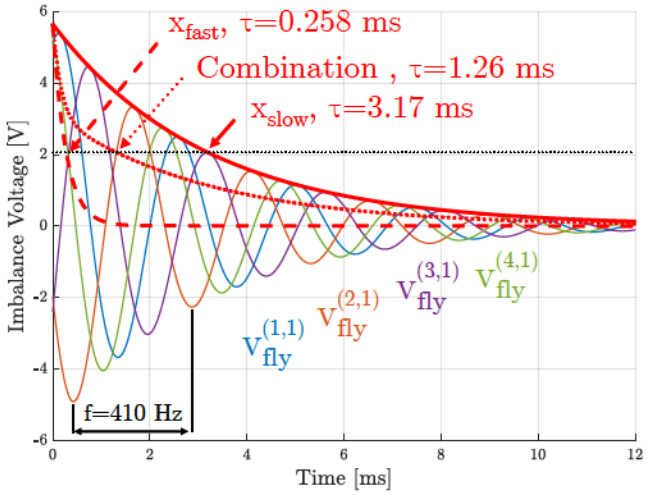

Fig. 9. Simulation of four-phase, three-level FCML converter balancing from different initial imbalances, demonstrating multi-resonant properties.

TABLE II
SIMULATION PARAMETERS OF THE FCML CONVERTER

f_{sw}	d	V_{dc}	C_{fly}	L_l	L_μ	R_w
500 kHz	0.5	16 V	50 μF	$\frac{1}{M^2}\mu H$	$100\times L_l$	10 mΩ

matrix $\mathbf{A}$ reveals the dynamics of FCML converter balancing. Through eigenanalysis, we can find the modes of imbalance decay and their relation to the starting imbalance $\tilde{\mathbf{x}}(0)$.

B. Effect of Initial Condition on FCML Converter Balancing

Like a higher-order single phase FCML converter, coupled inductor FCML converters can form damped resonant circuits when balancing. This happens because the flying capacitors exchange energy through the coupled inductors. We begin with the illustrative simulation of a four-phase, three-level converter with $f_{sw} = 500$ kHz, $d = 0.125$, $C_{fly} = 50$ μF, $L_l = 62.5$ nH, $C_o = 1$ mF, and $R_w = 50$ mΩ in Fig. 9. Eigenanalysis of the state-space matrix $\mathbf{A}$ for this converter reveals the system has three modes: a fast oscillatory mode with frequency 2.23 kHz and time constant 0.281 ms, a slow oscillatory mode with frequency 405 Hz and time constant 3.14 ms, and one quickly decaying R-L mode that is dominated by the other two.

The two oscillatory modes describe the ways the flying capacitor voltages can balance. In particular, the time constants show the time that it takes for the initial imbalance $\|\tilde{\mathbf{v}}_{\text{fly}}(0)\|$ to decay to $e^{-1}\times$ its original value. The two time constants are separated by an order of magnitude, which can have a major impact on the transient speed of the converter. The cause of the different balancing times is the initial condition. Depending on what the initial imbalances $\tilde{\mathbf{v}}_{\text{fly}}(0)$ are, different modes will be excited, which can result in drastically different balancing times. Thus, a converter with multiple flying capacitors can form a multi-resonant system where the initial condition affects the balancing dynamics.

Fig. 9 verifies the two predicted time constants by setting the four initial imbalances to those associated with the fast and slow modes. In both cases, the envelope of the imbalance

TABLE III
SIMULATED BALANCING TIME WITH COMMON-MODE AND DIFFERENTIAL-MODE IMBALANCES

# Phases M	1	2	4	6	8	16
$\tau_{\text{common-mode}}$ [ms]	60.1	7.44	1.53	1.29	0.61	0.061
$\tau_{\text{differential-mode}}$ [ms]	60.1	7.44	30.8	41.3	46.1	52.2

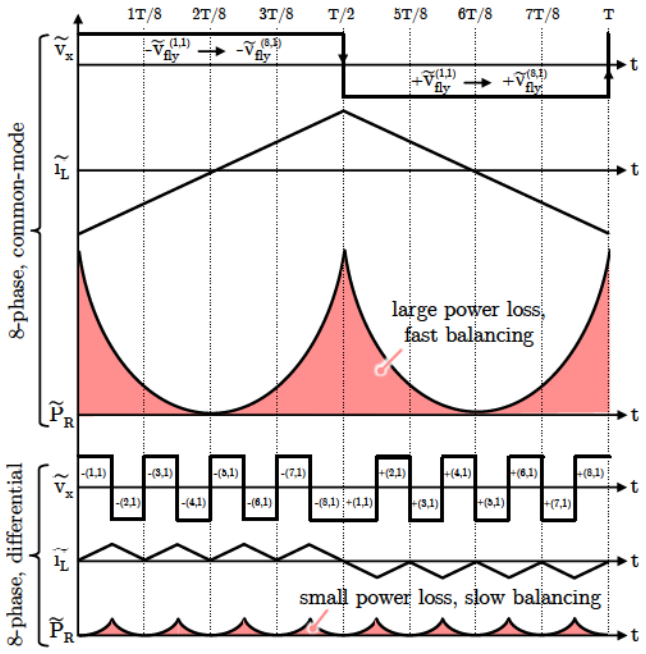

Fig. 10. Waveforms of an eight-phase converter with $d = \frac{1}{16}$ demonstrating the effect of a fast (common-mode) and slow (differential-mode) initial condition on the amount of imbalance energy dissipated in a period.

$\|\tilde{\mathbf{v}}_{\text{fly}}(t)\|$ decays exponentially with the predicted speed. If the initial condition is a combination of the two, then the decay is a combination of the two modes.

This analysis also reveals why the power dissipation model does not work for more complex FCML converters; a multi-resonant converter has multiple balancing modes. When computing the power dissipation model, we assumed a single exponential balancing mode, which cannot account for conditions where more than one mode is excited.

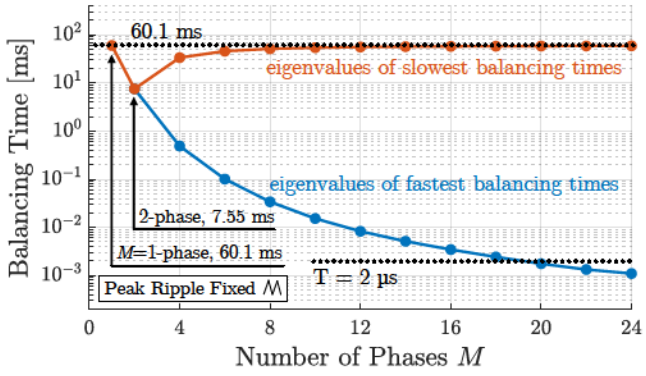

Fig. 11. Fastest and slowest eigenvalues of the balancing time of multiphase three-level FCML converters with ripple current held constant as the number of phases rises using the inductance parameters in Table II. The model predictions below the switching period $T = 2\ \mu s$ are included for completeness, but do invalidate the assumptions in Section III-B

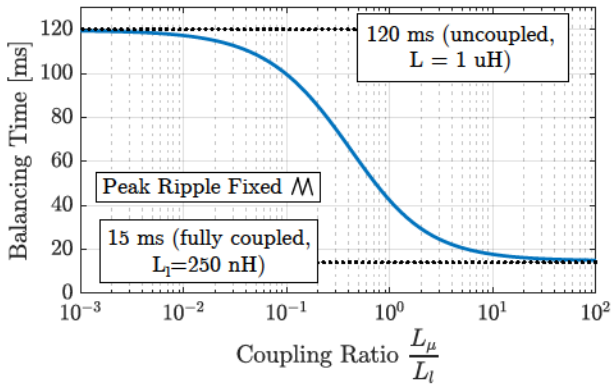

Fig. 12. PLECS simulation of balancing time vs. coupling ratio with parameters in Section III, with maximum per-phase current ripple fixed.

We consider two common cases for initial imbalances: (i) Common-Mode, where all initial imbalances are equal, such as during start-up or shut-down, and (ii) Differential-Mode, where the initial imbalance voltages are equal in magnitude and alternate in sign, which often results from external disturbances [43]. Using the circuit parameters shown in Table II, which keeps the maximum ripple current equal as the number of phases changes, we simulate the balancing time with a purely common-mode and differential imbalance for converters up to $M = 16$ phases. Except for the two-phase converter, which has only one mode, the common-mode time constant is always much smaller than the differential-mode case. The reason is illustrated in Fig. 10 with an eight-phase example. With a common-mode imbalance, the imbalance current and associated loss are large, which causes faster balancing. With a differential-mode imbalance, the switch node voltage constantly alternates, keeping the imbalance current and loss small, making the converter balance slower. Common-mode imbalances excite the leakage inductance and differential-mode imbalances excite the magnetizing inductance, which we is much larger for tightly coupled inductors [40]. The current is therefore much larger and lossier in the former case. As found before, only the one- and two- phase converters have a single balancing mode. Adding more phases introduces uncertainty in the balancing time depending on the imbalance. In the case that this uncertainty is undesirable, it would be better to use only a two-phase coupled inductor converter.

The slowest and fastest balancing modes predicted by the state-space model for for multiphase converters is shown in Fig. 11, where the maximum ripple current is kept constant between circuits. The slowest and fastest balancing time constants bound the possible balancing times, and other modes exist between them. The only converters with a deterministic balancing time are the one- and two-phase converters. In summary, the state-space model of coupled inductor FCML balancing dynamics shows the multi-resonant balancing properties dependent on the initial condition, and how slow and fast initial conditions can be predicted from the resultant loss.

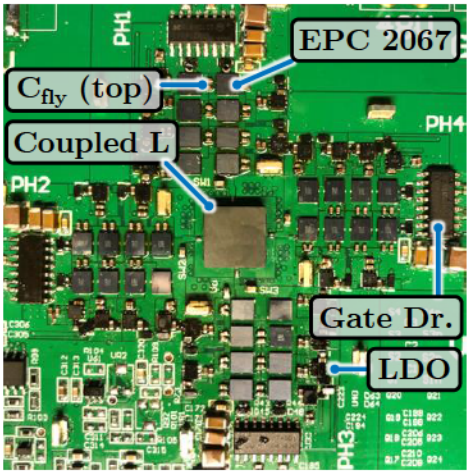

Fig. 13. Picture of the four-phase five-level FCML prototype with a four-phase coupled inductor implemented with PCB windings.

TABLE IV
CIRCUIT PARAMETERS OF THE FCML PROTOTYPE

Parameter/Component	Value
f_{sw}	500 kHz
V_{dc}	16 V
C_{fly}	1206 10 μF $\times$ 2
Custom Coupled Inductor L_l	23 & 192 nH
Custom Coupled Inductor L_μ	230 & 7.44 uH
Two-phase Coupled Inductor	Coilcraft PA6605-AL
Discrete Inductor	Coilcraft XAR7030-222MEB
Switches	EPC2067
Controller	EP4CE15F23C8

C. Model Limitations

The two balancing models presented in this work cover many common FCML converters, but they have some important limitations. First, the power dissipation model, while useful for relating the loss-context and balancing dynamics, only works in special circumstances where the loss is dependent only on the total normalized imbalance and not the specific imbalance in each flying capacitor. As mentioned before, this precludes its use for larger-order multi-resonant converters.

The state-space model is applicable to all converter sizes, but it suffers from elevated computational complexity and a lack of closed-form solutions. Additionally, the model assumes highly coupled inductors with high quality factor to simplify the calculations. As shown in [18], steady-state balancing analysis of fully-coupled inductors largely applies to moderately coupled inductors, with a smooth transition to the uncoupled solution. This occurs because even moderately coupled inductors share most of the inductive characteristics of fully coupled inductors. Fig. 12 shows the simulated balancing time of a two-phase, three-level FCML converter with varying coupling ratio and the peak ripple fixed. At the coupling extremities, the results match the model derived in Section III. The balancing time is similar to the fully-coupled solution even with moderate coupling ratios under $\frac{L_\mu}{L_l} < 10$.

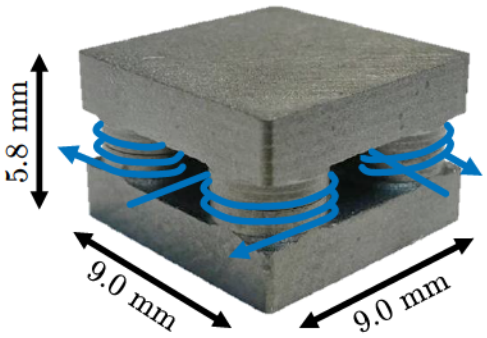

Fig. 14. Four-phase coupled inductor core using DMR53 material. The core consists of two identical halves pressed together from both sides of the PCB; the three-turn windings are formed by the PCB traces.

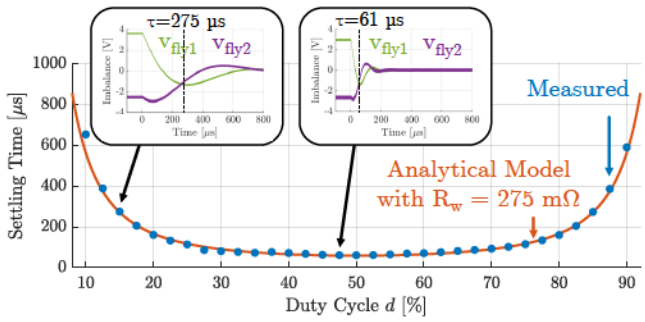

Fig. 15. Measured balancing time of a two-phase, three-level FCML converter compared to the power dissipation theoretical model. Each measured point represents a measurement of the time taken for the normalized imbalance to reduce to $e^{-1}\times$ the starting value.

V. EXPERIMENTAL VERIFICATION

To verify the theoretical balancing dynamics across converters with different numbers of phases, levels, switching frequencies, and coupling properties, we use the prototype shown in Fig. 13. The circuit parameters and components are listed in Table IV and the coupled inductor design is shown in Fig. 14. To introduce an initial imbalance, the phase shift between switches are deviated from their nominal values. This disturbance forces an imbalance voltage on the flying capacitors that depends on the phase shift applied to each phase [17], [36]. The disturbances are removed at time $t = 0$ and the flying capacitors dynamically balance to their nominal values. The balancing time is defined as the time taken for the normalized imbalance $\|\tilde{\mathbf{v}}_{\text{fly}}\|$ to decay to $e^{-1}\times$ of its starting value.

First, we verify the power dissipation model by measuring the balancing time of the two-phase, three-level converter with tightly coupled inductors and comparing it to the equation derived in eq. (22). The inductance, capacitance, switching frequency, and duty cycle are known or readily measured, but the effective R_w generating loss from the imbalance is not. To estimate R_w, we compare the power dissipated in the converter with and without an external imbalance. From here, we estimate the effective resistance that captures the imbalance-based loss is $R_w = 275$ mΩ. At each duty cycle in Fig. 15, the balancing time is measured and plotted against the analytical model with a good match.

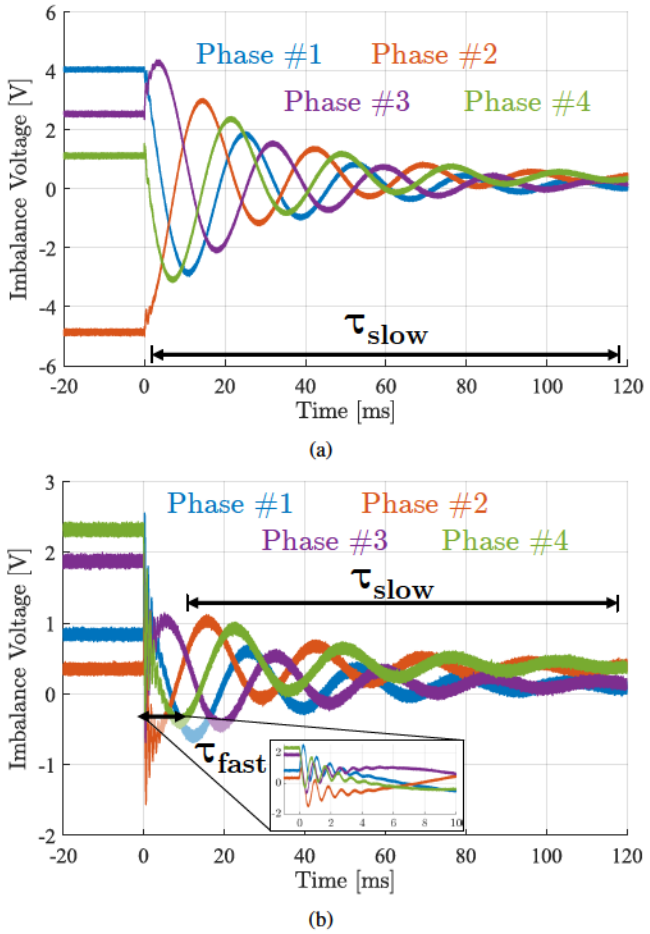

Fig. 16. Dynamic balancing of flying capacitors with initial conditions created by timing delays (a) $\mathbf{\Delta t_1} = \{73, 1, -87, 57\}$ ns and (b) $\mathbf{\Delta t_2} = \{-90, -100, -48, 65\}$ ns. Depending on the initial conditions, the voltages resonate with different frequencies and decay speeds.

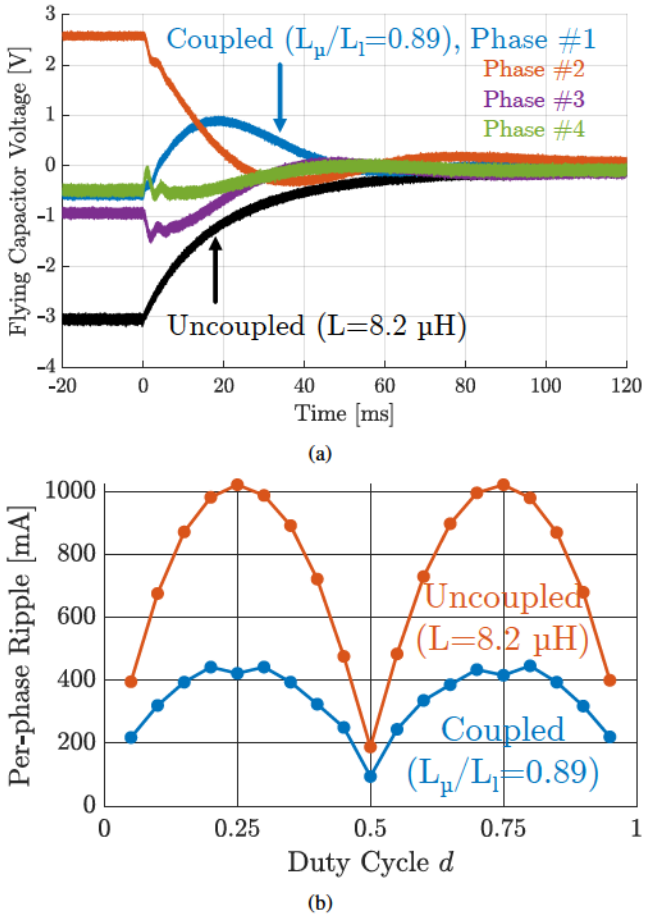

Fig. 17. (a) Flying capacitor balancing and (b) ripple of four-phase FCML converter with f_{sw} = 100 kHz. With loosely coupled inductors, the dynamic balancing is damped and the ripple is reduced compared to uncoupled inductors with inductance L = 8.2 μH equal to the leakage inductance.

Next, we verify the multi-resonant properties of a four-phase, three-level FCML converter with tightly coupled inductors. Fig. 16 shows balancing from two different initial conditions caused by external disturbances: (a) a time delay of $\mathbf{\Delta t_1} = \{73, 1, -87, 57\}$ ns for phases #1 through #4, and (b) $\mathbf{\Delta t_2} = \{-90, -100, -48, 65\}$ ns. The first imbalance almost exclusively contains components of the slowly decaying mode. The second imbalance contains components of both the fast and slow modes. The fast mode decays rapidly and oscillates at a high frequency. The difference between the two time constants is significant.

Even loosely or moderately coupled inductors still yield major improvements in ripple, transient response, and size, while having greater robustness to single-phase failure than tightly coupled inductors. Similarly, the dynamic balancing behavior changes depending on the coupling ratio. Fig. 17(a) shows the flying capacitors balancing from an initial imbalance created by a uniform delay of -140 ns in each phase. The uncoupled inductors have $L = 8.2\,\mu$H and switching frequency is reduced to 100 kHz. The coupled inductors have similar leakage inductance and a coupling ratio $\frac{L_\mu}{L_l} = 0.89$, significantly lower than the tightly coupled inductors used before. As a result, the oscillations are damped and the flying capacitors balance quickly. The time constant is similar to the uncoupled inductors since the leakage inductance is also approximately 8.2 μH. Fig. 17(b) shows the average per-phase ripple current of the uncoupled and loosely coupled converters. Therefore, the partially coupled inductors can simultaneously improve the ripple and steady-state imbalance without negatively affecting the balancing speed so long as the leakage inductance is kept constant.

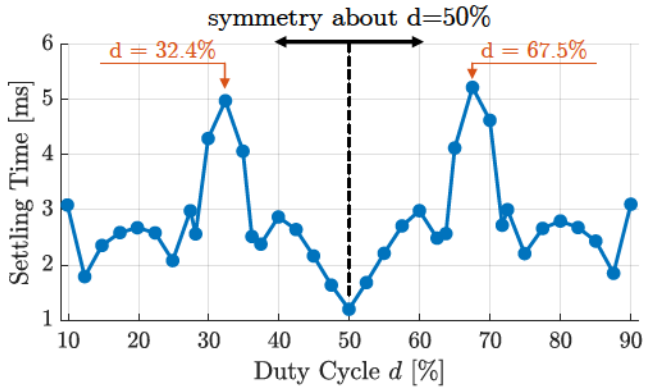

Fig. 18. Balancing time of normalized imbalance of four-phase converter across duty cycle range.

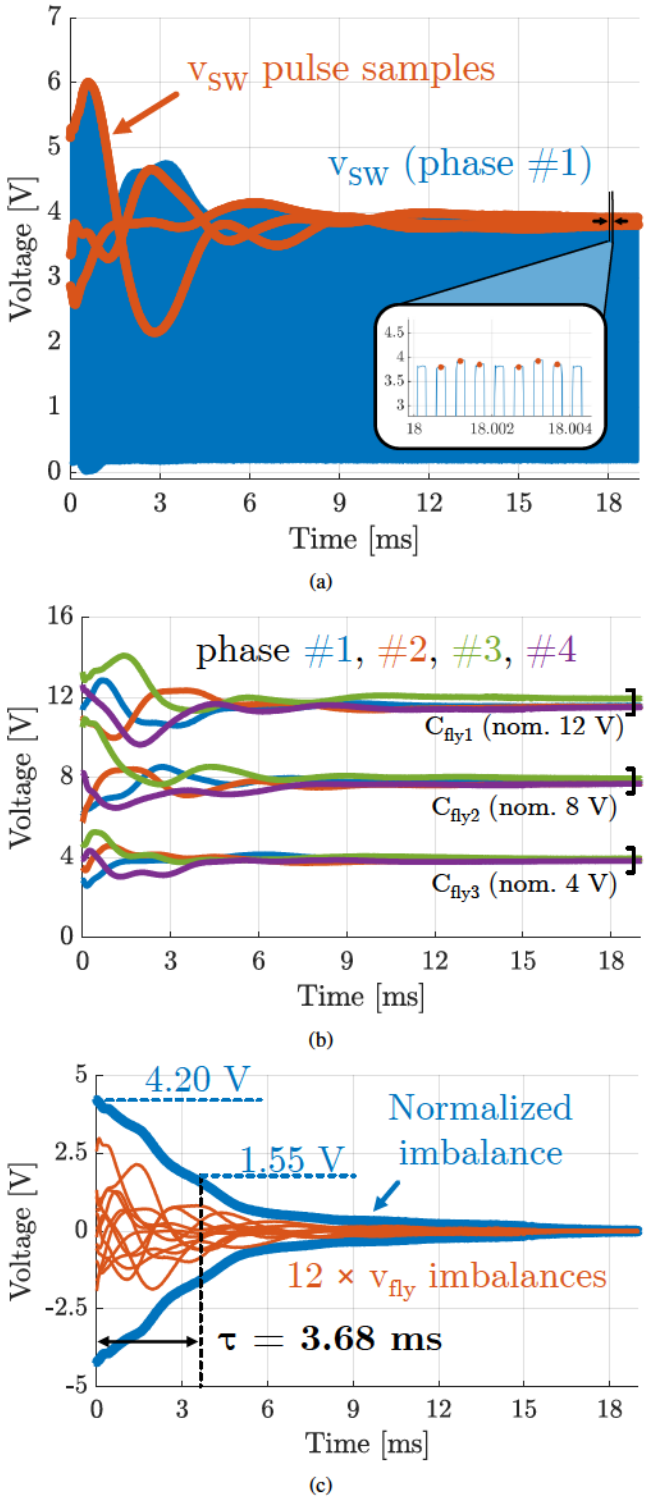

Fig. 19. (a) Raw switch node voltage measurement and sampling, (b) inference of flying capacitor voltages from switch node samples, and (c) conversion to imbalance components and normalized imbalance.

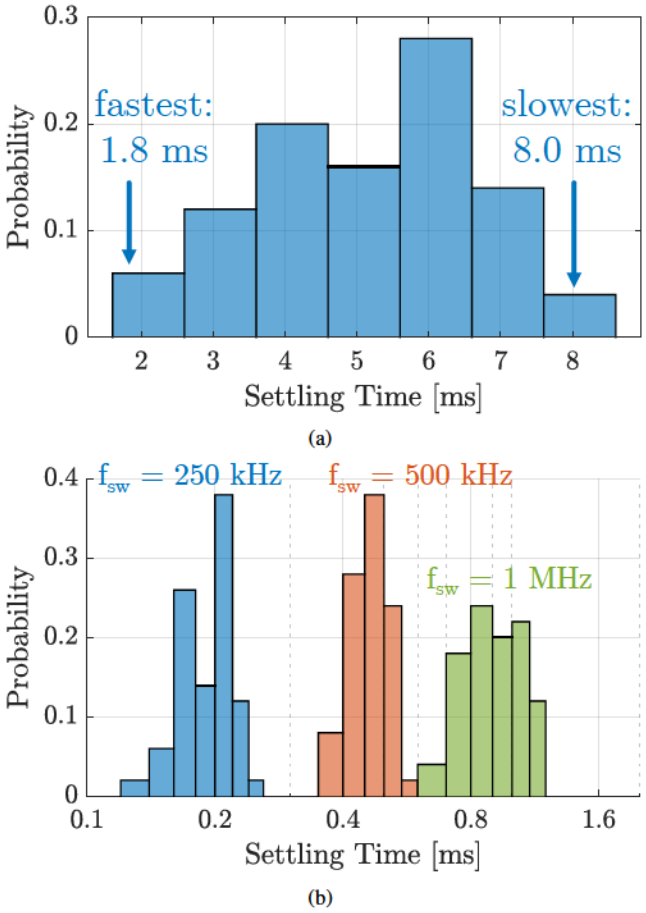

Fig. 20. (a) Histogram of experimentally measured balancing time at $d = 0.125$ and (b) with different switching frequencies.

Across the duty cycle range, the balancing time of a four-phase converter has a more complex trend, as shown in Fig. 18. The balancing time is still symmetric about $d = 0.5$, and two outlying points are aligned with singularities of coupled inductor balancing of four-phase converters [18].

As the number of phases, levels, and flying capacitors increases, the complexity of the balancing dynamics increases. To measure the 12 flying capacitor voltages for our four-phase, five-level prototype, we estimate them from the voltage pulses at the switch nodes. This is illustrated in Fig. 19(a). Like with the four-phase, three-level case, the capacitors start imbalanced and then oscillate to their balanced levels at 1/4, 1/2, and 3/4 of the input voltage, as shown in Fig 19(b). Finally, we find the balancing time in Fig. 19(c).

We use Monte Carlo analysis to study the balancing dynamics of the larger converter. In Fig. 20(a), the converter is operated at $f_{sw} = 500$ kHz and $d = 0.125$ with a random phase shift being applied to each of the set of switches between $\pm 7.2°$ over 50 trials. Due to the multi-resonance of the converter, the balancing time varies widely between 1.8 ms and 8 ms. The initial conditions significantly impact how fast a coupled FCML converter balances. Next, Fig. 20(b) shows the distribution of balancing times with the converter operating at $d = 0.375$ and three switching frequencies, with the same random phase shift on each set of switches. The balancing time again varies widely from minimum to maximum, and the balancing time increases as the frequency increases. This verifies the scaling of balancing time with frequency, and more fundamentally, the fact that balancing depends on the magnitude of loss that the imbalance generates.

VI. Conclusion

This paper develops dynamic models for coupled inductor FCML converter balancing. A model based on power dissipation is used for simple FCML converters to produce closed-form results that emphasize the importance of the loss-context on the balancing speed. A generalized state-space model is extended for coupled inductors of any number of phases and levels that reveals the multi-resonant behavior of FCML converter balancing, where the initial conditions determine the speed of balancing. Finally, the theoretical models are verified with detailed dynamic balancing experiments on FCML prototypes with varying switching frequencies, inductances, and numbers of phases and levels.

Acknowledgements

This work was supported by the National Science Foundation (Award #1847365) and the Natural Sciences and Engineering Research Council of Canada (Award #557270−2021).

Appendix I: Derivation of Power Dissipation Balancing Model

We restrict our analysis to three-level converters. There are generally $4M$ sub-periods, each with a different switching state. During each state, the inductor current is linearly ramped up or down by the connected flying capacitors. Because the starting current in each sub-period depends on the changes that occur in the preceding sub-periods, we define the current in each sub-period sequentially as

$$\tilde{i}_{L,\,j}(t) = \begin{cases} \frac{\mathbf{S_1}\tilde{\mathbf{v}}_{\text{fly}}}{L_l}t - \tilde{i}_{\text{offset}} & j = 1 \\ \tilde{i}_{L,\,j-1}\,|_{t=d^*T} + \frac{\mathbf{S_j}\tilde{\mathbf{v}}_{\text{fly}}}{L_l}t & j \text{ odd},\ j \neq 1 \\ \tilde{i}_{L,\,j-1}\,|_{t=d_{\text{rem}}T} + \frac{\mathbf{S_j}\tilde{\mathbf{v}}_{\text{fly}}}{L_l}t & j \text{ even}. \end{cases} \tag{27}$$

The switch state vector $\mathbf{S_j}$ is defined in Appendix II. The current in sub-period #1 ramps due to the connected flying capacitors, defined by $\mathbf{S_1}\tilde{\mathbf{v}}_{\text{fly}}$, minus a starting offset $\tilde{i}_{\text{offset}}$. The current in every subsequent sub-period is the current at the end of the previous sub-period plus a ramp. All the sub-period currents are assumed to start at $t = 0$ for simplicity. The initial condition for eq. (27) is found by setting the average inductor current to zero

$$\sum_{j=1}^{j=4M} \int_0^{t_j} \tilde{i}_{L,j}(t)\mathrm{d}t = 0 \tag{28}$$

and solving for the necessary offset current $\tilde{i}_{\text{offset}}$ which we substitute into eq. (27). The average power loss incurred in an unbalanced converter compared to a balanced converter is

$$\begin{aligned} R_w \left\langle i_L(t)^2 \right\rangle &= \frac{R_w}{T}\left[\sum_{j=1}^{j=4M} \int_0^{t_j} \tilde{i}_j(t)^2 \mathrm{d}t\right] \\ &= \frac{R_w T^2}{L_l^2} \times X\left(d, \tilde{\mathbf{v}}_{\text{fly}}(t)\right). \end{aligned} \tag{29}$$

The loss is a function of the duty cycle and flying capacitor voltages, which we represent with the function X. For a single-phase, three-level converter with $d < 0.5$ (mirrored for $d \geq 0.5$), the function is

$$X_{M=1} = \frac{d^2(3-4d)\tilde{v}_{\text{fly}}(t)^2}{12}. \tag{30}$$

For a two-phase, three-level converter with $d < 0.5$, it is

$$\begin{aligned} X_{M=2} &= \frac{d^2(3-4d)\left[(\tilde{v}_{\text{fly,1(t)}})^2 + (\tilde{v}_{\text{fly,2(t)}})^2\right]}{24} \\ &= \frac{d^2(3-4d)\|\tilde{\mathbf{v}}_{\text{fly}}(t)\|^2}{24}. \end{aligned} \tag{31}$$

Appendix II: Derivation of State-Space Model

To derive a generalized dynamic model for the flying capacitor voltages, we first define the relevant variables. If there are M phases and K flying capacitors per phase, there are $M \times K$ flying capacitor voltages

$$\tilde{\mathbf{v}}_{\text{fly}} = \begin{bmatrix} \tilde{v}_{\text{fly}}^{(1,1)} & \tilde{v}_{\text{fly}}^{(1,2)} & \cdots & \tilde{v}_{\text{fly}}^{(1,K)} & \tilde{v}_{\text{fly}}^{(2,1)} & \cdots & \tilde{v}_{\text{fly}}^{(M,K)} \end{bmatrix}^{\mathrm{T}}. \tag{32}$$

Ideally, the state vector $\tilde{\mathbf{v}}_{\text{fly}} = \mathbf{0}$ if there are no imbalances. The full state vector, defined below as $\tilde{\mathbf{x}}$, also includes one state for the inductor current for each phase:

$$\tilde{\mathbf{x}} = \begin{bmatrix} \tilde{\mathbf{v}}_{\text{fly}} \\ \tilde{i}_L \end{bmatrix}, \tag{33}$$

The flying capacitor voltages are connected differently during each switching state of the converter. To represent these changes, we define a switch state vector $\mathbf{\Phi_j}$ for each switching state as

$$\mathbf{\Phi_j} = \begin{bmatrix} \Phi_j^{(1,1)} & \cdots & \Phi_j^{(1,K+1)} & \Phi_j^{(2,1)} & \cdots & \Phi_j^{(M,K+1)} \end{bmatrix}, \tag{34}$$

where $\Phi_j^{(m,k'))}$ is the state of switch (m,k') for switching state j and is either 1 (ON) or 0 (OFF). $j = 1, 2, \ldots, 2M(K+1)$ denotes the switching state. From the switch state vector, we can determine how (or if) each flying capacitor is connected to the output during a given switching state. We let the flying capacitor state vector be

$$\mathbf{S_j} = \begin{bmatrix} S_j^{(1,1)} & S_j^{(1,2)} & \cdots & S_j^{(1,K)} & S_j^{(2,1)} & \cdots & S_j^{(M,K)} \end{bmatrix}, \tag{35}$$

where the flying capacitor with index (m,k) has connection

$$S_j^{(m,k)} = \Phi_j^{(m,k+1)} - \Phi_j^{(m,k)} \tag{36}$$

during sub-period j. If both adjacent switches have the same state, the capacitor is disconnected with $S_j^{(m,k)} = 0$. If not, $S_j^{(m,k)} = \pm 1$, representing the orientation of the flying capacitor. The sum of all the flying capacitor voltages connected to the output is

$$\tilde{v}_{\text{sum}} = \sum_{m=1}^{M}\sum_{k=1}^{K} S_j^{(m,k)}\tilde{v}_{\text{fly}}^{(m,k)} = \mathbf{S_j}\begin{bmatrix} \tilde{v}_{\text{fly}}^{(1,1)} \\ \tilde{v}_{\text{fly}}^{(1,2)} \\ \vdots \\ \tilde{v}_{\text{fly}}^{(M,K)} \end{bmatrix} \tag{37}$$

We now write the differential equations of the circuit, starting with the flying capacitors,

$$\frac{\mathrm{d}\tilde{v}_{\text{fly}}^{(m,k)}}{\mathrm{d}t} = -S_j^{(m,k)}\frac{1}{C_{\text{fly}}}\frac{\tilde{i}_L}{M}, \tag{38}$$

where the connection state $S_j^{(m,k)}$ determines if the capacitor charges or discharges. After the reduction in Fig. 8, we write the equation for the output network as

$$\tilde{v}_{\text{sum}} - L_l \frac{\mathrm{d}\tilde{i}_L}{\mathrm{d}t} - R_w \tilde{i}_L = 0. \tag{39}$$

Assuming at least one flying capacitor is connected to the output, we take the derivative of eq. (39) and substitute eqs. (37) and (38) into it, obtaining

$$\begin{aligned}
\sum_{m=1}^{M}\sum_{k=1}^{K} S_j^{(m,k)} \frac{\mathrm{d}\tilde{v}_{\text{fly}}^{(m,k)}}{\mathrm{d}t} - L_l \frac{\mathrm{d}^2\tilde{i}_L}{\mathrm{d}t^2} - R_w \frac{\mathrm{d}\tilde{i}_L}{\mathrm{d}t} &= 0 \\
\frac{\mathrm{d}^2\tilde{i}_L}{\mathrm{d}t^2} + \frac{R_w}{L_l}\frac{\mathrm{d}\tilde{i}_L}{\mathrm{d}t} + \frac{1}{L_l C_{\text{fly}} M}\tilde{i}_L \sum_{m=1}^{M}\sum_{k=1}^{K}\left|S_j^{(m,k)}\right| &= 0 \\
\frac{\mathrm{d}^2\tilde{i}_L}{\mathrm{d}t^2} + a\frac{\mathrm{d}\tilde{i}_L}{\mathrm{d}t} + b\tilde{i}_L &= 0,
\end{aligned} \tag{40}$$

where

$$a = \frac{R_w}{L_l}; b = \frac{1}{M L_l \left(C_{\text{fly}}/n_j\right)}. \tag{41}$$

Here, the term $n_j = \sum_{m=1}^{M}\sum_{k=1}^{K}\left|S_j^{(m,k)}\right|$ is the number of flying capacitors connected to the output during sub-period j, regardless of orientation. Equation (40) has the solution

$$\tilde{i}_L(t) = e^{-\frac{a}{2}t}\left[k_1\cos(\omega_d t) + k_2\sin(\omega_d t)\right], \tag{42}$$

where $\omega_d = \frac{1}{2}\sqrt{4b-a^2}$ and k_1 and k_2 are constants. k_1 is found by setting $t = 0$ for the beginning of the sub-period, $k_1 = \tilde{i}_L(0)$. Next, taking the derivative of eq. (42) and setting it equal to the initial change in inductor current $\frac{\mathrm{d}\tilde{i}_L(0)}{\mathrm{d}t}$, we solve for k_2 as

$$\begin{aligned}
\frac{\mathrm{d}\tilde{i}_L(0)}{\mathrm{d}t} = -\frac{a}{2}k_1 + k_2\omega_d &= \frac{1}{L_l}\left[\tilde{v}_{\text{sum}}(0) - R_w\tilde{i}_L(0)\right] \\
k_2 &= \frac{1}{L_l\omega_d}\tilde{v}_{\text{sum}}(0) - \frac{a}{2\omega_d}\tilde{i}_L(0).
\end{aligned} \tag{43}$$

Substituting the constants into into eq. (42), we find the solution for the inductor current in terms of the initial states

$$\tilde{i}_L(t) = \alpha(t)\tilde{v}_{\text{sum}}(t) + \beta(t)\tilde{i}_L(0), \tag{44}$$

where

$$\begin{aligned}
\alpha(t) &= \frac{1}{\omega_d L_l}e^{-\frac{a}{2}t}\sin(\omega_d t), \\
\beta(t) &= e^{-\frac{a}{2}t}\left[\cos(\omega_d t) - \frac{a}{2\omega_d}\sin(\omega_d t)\right].
\end{aligned} \tag{45}$$

If no flying capacitors are connected to the output, the inductor current simply decays exponentially through the resistance as $\tilde{i}_L(t) = \tilde{i}_L(0)e^{\frac{R_w}{L_l}t}$. We solve for the flying capacitor voltages by integrating the solution for the inductor current:

$$\begin{aligned}
\tilde{v}_{\text{fly}}^{(m,k)}(t) &= -\frac{S_j^{(m,k)}}{M C_{\text{fly}}}\int \tilde{i}_L \,\mathrm{d}t \\
&= A(t)\tilde{v}_{\text{sum}}(0) + B(t)\tilde{i}_L(0) + k_3,
\end{aligned} \tag{46}$$

where

$$\begin{aligned}
A(t) + d_1 &= -\frac{S_j^{(m,k)}}{M C_{\text{fly}}}\int \alpha(t)\,\mathrm{d}t \\
&= \frac{S_j^{(m,k)}}{n_j}e^{-\frac{a}{2}t}\left[\cos(\omega_d t) + \frac{a}{2\omega_d}\sin(\omega_d t)\right] + d_1,
\end{aligned} \tag{47}$$

$$\begin{aligned}
B(t) + d_2 &= -\frac{S_j^{(m,k)}}{M C_{\text{fly}}}\int \beta(t)\,\mathrm{d}t \\
&= -\frac{S_j^{(m,k)}}{M C_{\text{fly}}\omega_d}e^{-\frac{a}{2}t}\sin(\omega_d t) + d_2.
\end{aligned} \tag{48}$$

The constant k_3 absorbs the constants d_1 and d_2 in eq. (46) and is solved for at $t = 0$ as

$$k_3 = \tilde{v}_{\text{fly}}^{(m,k)}(0) + \frac{1}{n_j}\tilde{v}_{\text{sum}}(0). \tag{49}$$

Substituting eq. (49) into eq. (46), we find the solution for the flying capacitor voltage is

$$\tilde{v}_{\text{fly}}^{(m,k)}(t) = \tilde{v}_{\text{fly}}^{(m,k)}(0) + \left[A(t) + \frac{1}{n_j}\right]\tilde{v}_{\text{sum}}(0) + B(t)\tilde{i}_L(0). \tag{50}$$

Equation (44) and eq. (50) are used to update the inductor current and flying capacitor voltages from the initial states during a sub-period. In these equations, the time t refers to the time elapsed from when the sub-period begins at $t = 0$. Therefore, if we substitute $t = \Delta t_j$, where Δt_j is the duration of the sub-period, equations (44) and eq. (50) give the states at the end of the sub-period. Since an update equation exists for all the state variables, we can write a state transition equation

$$\mathbf{x}(\Delta t) = \mathbf{T_j}(\Delta t_j)\mathbf{x}(0), \tag{51}$$

where $\mathbf{T_j}(\boldsymbol{\Delta t})$ is the transition matrix for sub-period j. Note that the sub-period transition matrix is only dependent on the switch states and the other coefficients do not need to be recomputed. By computing the state transition matrix for every sub-period and multiplying them together in the order they occur, we can update the state variables from the beginning to the end of a period as

$$\mathbf{x}(T) = \left(\prod_{j=1}^{2M(K+1)}\mathbf{T_j}(\Delta t_j)\right)\mathbf{x}(0) = \mathbf{T}_{\text{full}}\mathbf{x}(0). \tag{52}$$

where Δt_j is the sub-period duration

$$\Delta t_j = \begin{cases} d^* T & j \text{ odd} \\ \left(\frac{1}{M(K+1)} - d^*\right)T & j \text{ even} \end{cases}. \tag{53}$$

To perform continuous-time analysis on the dynamic model, we use an approximation of the derivative assuming the balancing dynamics are much slower than the switching frequency. In this work, we use the second order central approximation of the derivative,

$$\frac{\mathrm{d}\mathbf{x}}{\mathrm{d}t} \approx \frac{-\mathbf{T}_{\text{full}}{}^2 + 8\mathbf{T}_{\text{full}} - 8\mathbf{T}_{\text{full}}{}^{-1} + (\mathbf{T}_{\text{full}}{}^{-1})^2}{12T}\mathbf{x}(t) = \mathbf{A}\mathbf{x}(t). \tag{54}$$

The continuous-time state matrix $\mathbf{A}$ determines the flying capacitor voltage balancing dynamics of the converter.

REFERENCES

[1] D. H. Zhou, Y. Elasser, and M. Chen, "Multi-resonant dynamics and voltage balancing of multiphase coupled inductor fcml converters," in *2023 IEEE Energy Conversion Congress and Exposition (ECCE)*, 2023, pp. 3607–3614.

[2] T. Meynard and H. Foch, "Multi-level conversion: high voltage choppers and voltage-source inverters," in *PESC '92 Record. 23rd Annual IEEE Power Electronics Specialists Conference*, 1992, pp. 397–403 vol.1.

[3] X. Zhou, P.-L. Wong, P. Xu, F. Lee, and A. Huang, "Investigation of candidate vrm topologies for future microprocessors," *IEEE Transactions on Power Electronics*, vol. 15, no. 6, pp. 1172–1182, 2000.

[4] J. Baek, Y. Elasser, K. Radhakrishnan, H. Gan, J. P. Douglas, H. K. Krishnamurthy, X. Li, S. Jiang, C. R. Sullivan, and M. Chen, "Vertical stacked lego-pol cpu voltage regulator," *IEEE Transactions on Power Electronics*, vol. 37, no. 6, pp. 6305–6322, 2022.

[5] J. Böhler, J. Huber, J. Wurz, M. Stransky, N. Uvaidov, S. Srdic, and J. W. Kolar, "Ultra-high-bandwidth power amplifiers: A technology overview and future prospects," *IEEE Access*, vol. 10, pp. 54 613–54 633, 2022.

[6] O. García, M. Vasić, P. Alou, J. Oliver, and J. A. Cobos, "An overview of fast dc–dc converters for envelope amplifier in rf transmitters," *IEEE Transactions on Power Electronics*, vol. 28, no. 10, pp. 4712–4722, 2013.

[7] B. P. McGrath and D. G. Holmes, "Enhanced voltage balancing of a flying capacitor multilevel converter using phase disposition (pd) modulation," *IEEE Transactions on Power Electronics*, vol. 26, no. 7, pp. 1933–1942, 2011.

[8] V. Lazarević, "Ultra-fast and compact gan-based power amplifier as an arbitrary voltage generator," Ph.D. dissertation, Universidad Politécnica de Madrid, 2021.

[9] P. S. Niklaus, J. W. Kolar, and D. Bortis, "100 khz large-signal bandwidth gan-based 10 kva class-d power amplifier with 4.8 mhz switching frequency," *IEEE Transactions on Power Electronics*, vol. 38, no. 2, pp. 2307–2326, 2023.

[10] C. B. Barth, P. Assem, T. Foulkes, W. H. Chung, T. Modeer, Y. Lei, and R. C. N. Pilawa-Podgurski, "Design and control of a gan-based, 13-level, flying capacitor multilevel inverter," *IEEE Journal of Emerging and Selected Topics in Power Electronics*, vol. 8, no. 3, pp. 2179–2191, 2020.

[11] T. Modeer, C. B. Barth, N. Pallo, W. H. Chung, T. Foulkes, and R. C. N. Pilawa-Podgurski, "Design of a gan-based, 9-level flying capacitor multilevel inverter with low inductance layout," in *2017 IEEE Applied Power Electronics Conference and Exposition (APEC)*, 2017, pp. 2582–2589.

[12] N. C. Brooks, J. Zou, S. Coday, T. Ge, N. M. Ellis, and R. C. N. Pilawa-Podgurski, "On the size and weight of passive components: Scaling trends for high-density power converter designs," *IEEE Transactions on Power Electronics*, vol. 39, no. 7, pp. 8459–8477, 2024.

[13] R. Wilkinson, H. du Mouton, and T. Meynard, "Natural balance of multicell converters," in *IEEE 34th Annual Conference on Power Electronics Specialist, 2003. PESC '03.*, vol. 3, 2003, pp. 1307–1312 vol.3.

[14] R. H. Wilkinson, T. A. Meynard, and H. du Toit Mouton, "Natural balance of multicell converters: The two-cell case," *IEEE Transactions on Power Electronics*, vol. 21, no. 6, pp. 1649–1657, 2006.

[15] R. H. Wilkinson, T. A. Meynard, and H. du Toit Mouton, "Natural balance of multicell converters: The general case," *IEEE Transactions on Power Electronics*, vol. 21, no. 6, pp. 1658–1666, 2006.

[16] B. P. McGrath and D. G. Holmes, "Analytical modelling of voltage balance dynamics for a flying capacitor multilevel converter," in *2007 IEEE Power Electronics Specialists Conference*, 2007, pp. 1810–1816.

[17] Z. Ye, Y. Lei, Z. Liao, and R. C. N. Pilawa-Podgurski, "Investigation of capacitor voltage balancing in practical implementations of flying capacitor multilevel converters," *IEEE Transactions on Power Electronics*, vol. 37, no. 3, pp. 2921–2935, 2022.

[18] D. H. Zhou, J. Čeliković, D. Maksimović, and M. Chen, "Balancing multiphase fcml converters with coupled inductors: Modeling, analysis, limitations," *IEEE Transactions on Power Electronics*, pp. 1–24, 2024.

[19] A. Ruderman and B. Reznikov, "Five-level single-leg flying capacitor converter voltage balance dynamics analysis," in *2009 35th Annual Conference of IEEE Industrial Electronics*, 2009, pp. 486–491.

[20] S. Thielemans, A. Ruderman, and J. Melkebeek, "Flying-capacitor multilevel converter voltage balance dynamics for pure resistive load," in *2009 8th International Symposium on Advanced Electromechanical Motion Systems Electric Drives Joint Symposium*, 2009, pp. 1–6.

[21] S. Thielemans, A. Ruderman, B. Reznikov, and J. Melkebeek, "Improved natural balancing with modified phase-shifted pwm for single-leg five-level flying-capacitor converters," *IEEE Transactions on Power Electronics*, vol. 27, no. 4, pp. 1658–1667, 2012.

[22] J. S. Rentmeister and J. T. Stauth, "Modeling the dynamic behavior of hybrid-switched-capacitor converters in state space," in *2018 IEEE 19th Workshop on Control and Modeling for Power Electronics (COMPEL)*, 2018, pp. 1–7.

[23] N. C. Brooks, R. K. Iyer, R. S. Bayliss, and R. C. N. Pilawa-Podgurski, "Fundamental state-space modeling methodology for the flying capacitor multilevel converter," in *2022 IEEE 23rd Workshop on Control and Modeling for Power Electronics (COMPEL)*, 2022, pp. 1–7.

[24] R. S. Bayliss, N. C. Brooks, and R. C. N. Pilawa-Podgurski, "On the role of switch output capacitance on passive balancing within the flying capacitor multilevel converter," in *2022 IEEE 23rd Workshop on Control and Modeling for Power Electronics (COMPEL)*, 2022, pp. 1–6.

[25] Z. Xia and J. T. Stauth, "Constant switch stress control of hybrid switched capacitor dc-dc converters," in *2022 IEEE Applied Power Electronics Conference and Exposition (APEC)*, 2022, pp. 1214–1221.

[26] Z. Xia, B. L. Dobbins, J. S. Rentmeister, and J. T. Stauth, "State space analysis of flying capacitor multilevel dc-dc converters for capacitor voltage estimation," in *2019 IEEE Applied Power Electronics Conference and Exposition (APEC)*, 2019, pp. 50–57.

[27] Z. Xia, K. Datta, and J. T. Stauth, "State-space modeling and control of flying-capacitor multilevel dc–dc converters," *IEEE Transactions on Power Electronics*, vol. 38, no. 10, pp. 12 288–12 303, 2023.

[28] K. Datta and J. T. Stauth, "Comparison of voltage balance and state estimation dynamics for hybrid switched-capacitor converter topologies," in *2023 IEEE 24th Workshop on Control and Modeling for Power Electronics (COMPEL)*, 2023, pp. 1–8.

[29] J. Celikovic, R. Das, H.-P. Le, and D. Maksimovic, "Modeling of capacitor voltage imbalance in flying capacitor multilevel dc-dc converters," in *2019 20th Workshop on Control and Modeling for Power Electronics (COMPEL)*, 2019, pp. 1–8.

[30] Z. Xia, B. L. Dobbins, and J. T. Stauth, "Natural balancing of flying capacitor multilevel converters at nominal conversion ratios," in *2019 20th Workshop on Control and Modeling for Power Electronics (COMPEL)*, 2019, pp. 1–8.

[31] L. Corradini and D. Maksimović, "Steady-state indeterminacy in lossless switched-mode power converters," *IEEE Transactions on Power Electronics*, vol. 38, no. 3, pp. 3001–3013, 2023.

[32] D. H. Zhou and M. Chen, "Switching frequency is not the limit: Multiphase coupled inductor fcml converter tracking signals above the switching frequency," in *2023 IEEE 24th Workshop on Control and Modeling for Power Electronics (COMPEL)*, 2023, pp. 1–7.

[33] S. Coday, A. Barchowsky, and R. C. Pilawa-Podgurski, "A 10-level gan-based flying capacitor multilevel boost converter for radiation-hardened operation in space applications," in *2021 IEEE Applied Power Electronics Conference and Exposition (APEC)*, 2021, pp. 2798–2803.

[34] A. Stillwell, E. Candan, and R. C. N. Pilawa-Podgurski, "Active voltage balancing in flying capacitor multi-level converters with valley current detection and constant effective duty cycle control," *IEEE Transactions on Power Electronics*, vol. 34, no. 11, pp. 11 429–11 441, 2019.

[35] J. S. Rentmeister and J. T. Stauth, "A 48v:2v flying capacitor multilevel converter using current-limit control for flying capacitor balance," in *2017 IEEE Applied Power Electronics Conference and Exposition (APEC)*, 2017, pp. 367–372.

[36] D. H. Zhou, J. Celikovic, Y. Elasser, D. Maksimovic, and M. Chen, "Balancing limits of flying capacitor voltages in coupled inductor fcml converters," in *2022 IEEE 23rd Workshop on Control and Modeling for Power Electronics (COMPEL)*, 2022, pp. 1–8.

[37] P.-L. Wong, P. Xu, P. Yang, and F. Lee, "Performance improvements of interleaving vrms with coupling inductors," *IEEE Transactions on Power Electronics*, vol. 16, no. 4, pp. 499–507, 2001.

[38] P.-L. Wong, "Performance improvements of multi-channel interleaving voltage regulator modules with integrated coupling inductors," Ph.D. dissertation, Virginia Tech,, 2001.

[39] M. Chen and C. R. Sullivan, "Unified models for coupled inductors applied to multiphase pwm converters," *IEEE Transactions on Power Electronics*, vol. 36, no. 12, pp. 14 155–14 174, 2021.

[40] D. H. Zhou, Y. Elasser, J. Baek, and M. Chen, "Reluctance-based dynamic models for multiphase coupled inductor buck converters," *IEEE Transactions on Power Electronics*, vol. 37, no. 2, pp. 1334–1351, 2022.

[41] N. Brooks, "Hybrid switched-capacitor converter design: State-space dynamical modeling and passive device characterization," Ph.D. dissertation, 2023 2023, copyright - Database copyright ProQuest LLC; ProQuest does not claim copyright in the individual underlying works; Last updated - 2023-10-20.

[42] T. Meynard, M. Fadel, and N. Aouda, "Modeling of multilevel converters," *IEEE Transactions on Industrial Electronics*, vol. 44, no. 3, pp. 356–364, 1997.

[43] D. H. Zhou, A. Bendory, C. Li, and M. Chen, "Multiphase fcml converter with coupled inductors for ripple reduction and intrinsic flying capacitor voltage balancing," in *2022 IEEE Applied Power Electronics Conference and Exposition (APEC)*, 2022, pp. 1284–1290.

Daniel H. Zhou (Student Member, IEEE) received the B.A.Sc degree in mechatronics engineering from the University of Waterloo, Waterloo, Canada, in 2019. He received the M.A. degree in electrical engineering from Princeton University, Princeton, NJ, USA in 2021 and is currently working towards the Ph.D. degree.

His research interests include ultrafast power converters, multilevel converters, and advanced power magnetics design. Mr. Zhou is a recipient of the IEEE PELS John G. Kassakian Fellowship and the Natural Sciences and Engineering Research Council of Canada (NSERC) Alexander Graham Bell Graduate Scholarship. He is also an awardee of the Princeton School of Engineering and Applied Science Honorific Fellowship and Graduate Student Award for Excellence in Service.

Minjie Chen (Senior Member, IEEE) received the S.M., E.E., and Ph.D. degrees in electrical engineering and computer science from Massachusetts Institute of Technology, Cambridge, MA, USA, in 2015 and the B.S. degree in electrical engineering from Tsinghua University, Beijing, China, in 2009. He is an Associate Professor of Electrical and Computer Engineering and the Andlinger Center for Energy and the Environment at Princeton University. His research interests include modeling, design, and application of high-performance power electronics.

Dr. Chen is the recipient of the IEEE PELS Richard M. Bass Outstanding Young Power Electronics Engineer Award, the Princeton SEAS E. Lawrence Keyes, Jr./Emerson Electric Co. Junior Faculty Award, the NSF CAREER Award, seven IEEE Transactions on Power Electronics Prize Paper Awards, the C3.ai Faculty Award, the Princeton Innovation Award, the ASAE Power of Associations Silver Award, the MIT EECS D. N. Chorafas Ph.D. Thesis Award, and numerous conference Best Paper Awards from COMPEL, ICRA, IROS, ECCE, APEC, 3D-PEIM, and OCP. He was listed on the Princeton Engineering Commendation List for Outstanding Teaching multiple times. He is an Associate Editor of the IEEE Transactions on Power Electronics and the IEEE Journal of Emerging and Selected Topics in Power Electronics. He is an IEEE PELS Distinguished Lecturer, the vice chair of IEEE PELS TC10-Design Methodologies, and has launched the IEEE PELS MagNet Challenge.